

Learning-Based Quality Control for Cardiac MR Images

Giacomo Tarroni, Ozan Oktay, Wenjia Bai, Andreas Schuh, Hideaki Suzuki, Jonathan Passerat-Palmbach, Ben Glocker, Paul M. Matthews, Daniel Rueckert

Abstract—The effectiveness of a cardiovascular magnetic resonance (CMR) scan depends on the ability of the operator to correctly tune the acquisition parameters to the subject being scanned and on the potential occurrence of imaging artefacts such as cardiac and respiratory motion. In clinical practice, a quality control step is performed by visual assessment of the acquired images: however, this procedure is strongly operator-dependent, cumbersome and sometimes incompatible with the time constraints in clinical settings and large-scale studies. We propose a fast, fully-automated, learning-based quality control pipeline for CMR images, specifically for short-axis image stacks. Our pipeline performs three important quality checks: 1) heart coverage estimation, 2) inter-slice motion detection, 3) image contrast estimation in the cardiac region. The pipeline uses a hybrid decision forest method - integrating both regression and structured classification models - to extract landmarks as well as probabilistic segmentation maps from both long- and short-axis images as a basis to perform the quality checks. The technique was tested on up to 3000 cases from the UK Biobank study and validated against manual annotations and visual inspections performed by expert interpreters. The results show the capability of the proposed pipeline to correctly detect incomplete or corrupted scans, allowing their exclusion from the analysed dataset or the triggering of a new acquisition.

Index Terms—Image quality assessment, Magnetic resonance imaging, Motion compensation and analysis, Heart

I. INTRODUCTION

CARDIOVASCULAR magnetic resonance (CMR) imaging presents a wide variety of different applications for the anatomical and functional assessment of the heart. The success of a CMR acquisition relies, however, on the ability of the MR operator to correctly tune the acquisition parameters to the subject being scanned [1]. Moreover, CMR can be negatively affected by a long list of imaging artefacts (caused for instance by respiratory and cardiac motion, blood flow and magnetic field inhomogeneities) [2]. Therefore, a quality control step is required to assess the usability of the acquired images. In clinical practice this step is performed by visual inspection, usually carried out by the same operator who set up the acquisition, thus leading to highly subjective results. In the last decades, several initiatives for the acquisition of open access large-scale population studies have been launched. For example, the UK Biobank (UKBB) is a population-based

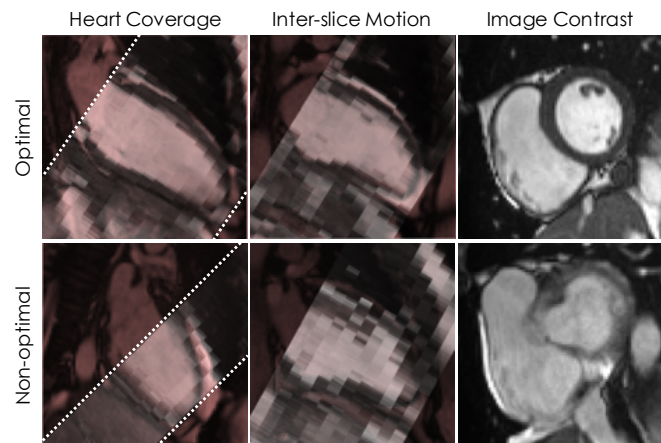


Fig. 1: Potential issues affecting CMR image acquisitions. In the first two columns, mixed views of long-axis two-chamber views (red) and short-axis stacks (gray) are shown, while in the last one short-axis slice are displayed.

prospective study, established to allow detailed investigations of the genetic and non-genetic determinants of the diseases of middle and old age. Of the 500,000 subjects enrolled in the study, CMR will be collected from 100,000 of them [3]. At the time of submission the acquisition is ongoing, with close to 20,000 subjects already scanned. Together with this trend towards the implementation of large-scale multi-centre imaging datasets, the need for fast and reliable quality control techniques for CMR images has become evident, as highlighted also by several studies aiming to define standardized criteria for this task [4]. In this scenario, quality control through visual inspection is not only subjective, but simply infeasible due to the very high throughput demanded by the acquisition pipeline. On the other hand, failure to correctly identify corrupted or unusable images might affect the results of automated analysis performed on the dataset, with undesirable effects. Consequently, the need for fully automated quality control pipelines for CMR images has arisen.

Several research efforts have been dedicated to the automated identification of quality metrics from MR images. Most of these efforts have focused on the automated estimation of noise levels [5], [6]. Still, many aspects related to the usability of the acquired images are inherently modality-specific. As far as brain MR imaging is concerned, several automated pipelines for quality control have been proposed [7]. However, to our knowledge, no comprehensive automated quality control

G. Tarroni is with the Department of Computing, Imperial College London, SW7 2AZ London, UK, e-mail: giacomo.tarroni@gmail.com. O. Oktay, W. Bai, A. Schuh, J. Passerat-Palmbach, B. Glocker and D. Rueckert are also with the Department of Computing, Imperial College London.

H. Suzuki and P. M. Matthews are with the Division of Brain Sciences, Department of Medicine, Imperial College London. P. M. Matthews is also with the UK Dementia Research Institute, London, UK.

pipelines have been proposed so far for CMR images, in particular for the short-axis (SA) cine image stacks, which are the reference images for the structural and functional assessment of the heart. One crucial aspect of the acquisition of SA image stacks is that it requires the MR operator to identify the direction of the left ventricular (LV) long axis, which is the line going from the apex to the centre of the mitral valve, and to define a region of interest: the correct planning will generate a SA stack encompassing both those landmarks with slices perpendicular to the LV long axis. If this selection is incorrect, the acquired SA stack may include an insufficient number of SA slices to fully cover the LV (see first column of Fig. 1). As a consequence, any functional analysis performed on the stack (e.g. ventricular volumes estimation) may be compromised. Another important aspect involved in CMR acquisitions is that SA cine stacks are generated during multiple breath-holds (with usually 1-3 slices acquired per each breath-hold). Although the subjects are instructed to hold their breath at the same breath-hold position, in practice the heart location can vary considerably. If the differences between the breath-hold positions are too pronounced, the acquired image stack will be affected by inter-slice motion and thus not correctly represent the cardiac volume, introducing potential errors in the following analyses and visualizations (see second column of Fig. 1). Finally, the contrast of the obtained image is directly affected by the chosen acquisition parameters (as well as by potential artefacts). If the different structures of the heart are not properly contrasted, the assessment of the cardiac function can be hampered (see third column of Fig. 1).

In this paper, we present a learning-based approach to fully-automated quality control for CMR SA image stacks. Our approach uses a hybrid decision forest method to extract landmarks (LMs) as well as probabilistic segmentation maps (PSMs) from both long-axis (LA) and SA images. LMs and PSMs are then used to perform three quality checks: 1) heart coverage estimation, 2) inter-slice motion detection, 3) image contrast estimation in the cardiac region. The technique was tested on up to 3000 cases from the UKBB study and validated against manual annotations and visual inspections.

II. RELATED WORK

To the best of our knowledge, differently from brain MRI [7], no comprehensive quality control techniques for cardiac CMR images have been reported in the literature. One of the few studies in this direction has been recently presented by Alba et al. [8], who however focussed on quality assessment of the segmentations instead of the images themselves. On the other hand, automated heart coverage estimation alone has been the aim of several studies. Zhang et al. [9], [10] proposed to use convolutional neural networks (CNN) to perform slice classification in order to detect the presence or absence of the most basal and most apical slices. In their first work [9] they proposed a 2D CNN trained on UKBB data, while in their more recent one [10] they improved their previous results by using a generative adversarial network. Differently from these techniques, our approach to heart coverage estimation is based on the detection of landmarks: in our previous preliminary

work [11], we proposed a decision forest method to detect the cardiac apex and the mitral valve on long-axis 2-chamber (LA 2CH) view images, and used the position of these landmarks with respect to the space encompassed by the acquired stack to estimate the coverage. The technique was applied to 3000 cases extracted from the UKBB, and was able to detect SA stacks with insufficient coverage with relatively high accuracy.

We have been unable to find any techniques in the literature focussing specifically on inter-slice respiratory motion detection. Instead, many approaches for inter-slice motion correction have been reported in the last decade [12], [13], [14], [15]. It is important to note that all of the aforementioned studies focused on the compensation of inter-slice motion and in the generation of a corrected SA stack by means of rigid in-plane registration. Unfortunately, however, respiration causes a complex roto-translation of the heart in all three dimensions [16]: while most translation happens in the cranio-caudal direction (thus approximately almost perpendicularly to the long axis of the LV), big differences in subsequent breath-hold positions can cause out-of-plane motion, which would lead to an inaccurate representation of the heart in the stack. As a consequence, it is important to estimate the amount of motion occurred during the acquisition of the stack in order to decide whether there are the grounds for the application of a motion correction technique or it is instead advisable to repeat the scan or exclude it from subsequent analyses.

In the past, several research efforts have been made towards the correct quantification of signal-to-noise (SNR) or contrast-to-noise (CNR) ratios in MR images [5]. However, modern acquisition techniques making use of parallel imaging produce images with spatially-varying noise distributions, making image-based estimators unreliable [17]. To overcome this limitation, more elaborate methods have been proposed exploiting information about coil sensitivity or reconstruction coefficients [18]. Unfortunately, these data are very often not available, making the estimation of noise, and consequently of SNR and CNR, practically unfeasible in most scenarios. At the same time, image contrast between two objects - simply defined as the difference between their signal intensity - has long been used to determine their visual differentiability in the acquired MR image [19]. In CMR imaging, images with poor contrast between the LV cavity and myocardium can potentially hinder the assessment of cardiac structure and function: consequently, contrast estimation in the cardiac region can provide a useful metric for quality control purposes, either triggering the use of contrast-enhancing techniques or a new acquisition.

In this paper, we present a fully automated learning-based quality control pipeline for CMR SA stacks. Our pipeline uses a hybrid decision forest method which builds upon the design we previously presented for landmark detection [20]. Specifically, while the forest design presented in that study was able to extract landmark positions and probabilistic edge maps (PEMs) also adopted in motion correction techniques [13], the new implementation allows the extraction of landmark positions (LMs) and probabilistic segmentation maps (PSMs), which will be adopted for both inter-slice motion detection and cardiac image contrast estimation. In summary, the main contributions of the present work can be listed as follows:

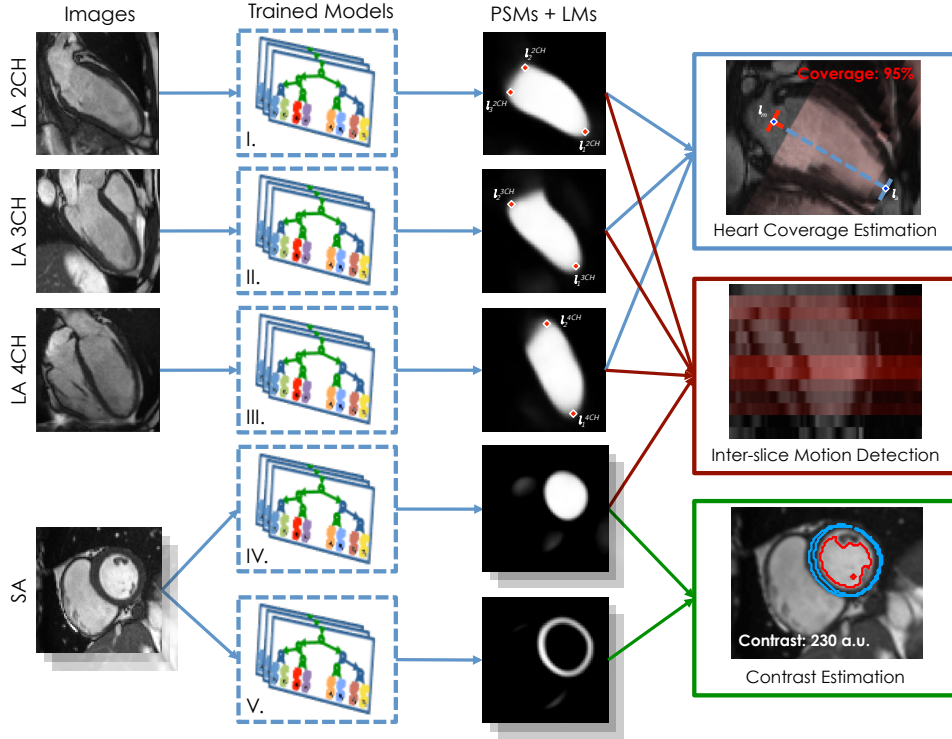


Fig. 2: Overview of the proposed pipeline. Probabilistic segmentation maps (PSMs) and landmarks (LMs) are extracted from LA and SA images using hybrid random forests and exploited to perform three separate quality control checks.

- We present the first comprehensive, fast, fully-automated quality control pipeline specifically designed for CMR SA image stacks. The checks incorporated in the pipeline are 1) heart coverage estimation, 2) inter-slice motion detection, 3) image contrast estimation in the cardiac region. To the best of our knowledge, motion detection and cardiac image contrast have not been investigated before. As for heart coverage estimation, we build on our previously published study [11] by extending the landmark extraction to all of the long-axis views;
- We propose a different implementation of the previously published hybrid decision forest [20] that allows the joint extraction of landmark positions and of PSMs. PSMs enable cardiac image contrast estimation and a more robust inter-slice motion detection, and could be adopted for a variety of other image analysis tasks;
- We validate this pipeline by applying it to up to 3000 cases extracted from the UKBB study, showing its accuracy and robustness in a real world scenario. The pipeline could be both applied retrospectively on large-scale datasets to improve the reliability of clinical studies and deployed prospectively at acquisition sites to allow almost real-time assessment of the acquired scans.

III. METHODS

The proposed quality control pipeline is summarized in Fig. 2. All of the three quality control steps are based on the information extracted by hybrid decision forest models from the acquired images. This section of the paper starts with a brief recap on the theory behind decision forests and

is followed by the description of the implementation adopted in the proposed pipeline, which allows the joint estimation of LMs and PSMs. Finally, each specific quality control step is described in detail.

A. Hybrid Decision Forests

A decision tree consists of a combination of split and leaf nodes arranged in a tree-like structure [21]. Decision trees route a sample $\mathbf{x} \in \mathcal{X}$ (in our case an image patch) by recursively branching left or right at each split node j until a leaf node k is reached. Each leaf node is associated with a posterior distribution $p(y|\mathbf{x})$ for the output variable $y \in \mathcal{Y}$. Each split node j is associated with a binary split function $h(\mathbf{x}, \theta_j) \in \{0, 1\}$ defined by the set of parameters θ_j : if the outcome is 0 the node sends \mathbf{x} to the left, otherwise to the right. In most cases, h is a decision stump, i.e. a single feature dimension n of \mathbf{x} is compared with a threshold τ : $\theta = (n, \tau)$ and $h(\mathbf{x}, \theta) = [\mathbf{x}(n) < \tau]$. A decision forest is an ensemble of T independent decision trees: during testing, given a sample patch \mathbf{x} , the predictions of the different trees are combined into a single output using an ensemble model. During training, at each node the goal is to find the set of parameters θ_j which maximizes a previously defined information gain I_j , that is usually defined as $I_j = H(S_j) - \sum_{i \in \{0,1\}} |S_j^i|/|S_j| \cdot H(S_j^i)$, where S_j , S_j^0 and S_j^1 are respectively the training set (comprising of samples \mathbf{x} and associated labels y) arriving at node j , leaving the node to the left and to the right. $H(S)$ is the entropy of the training set, whose construction depends on the task at hand (e.g. classification, regression). Different

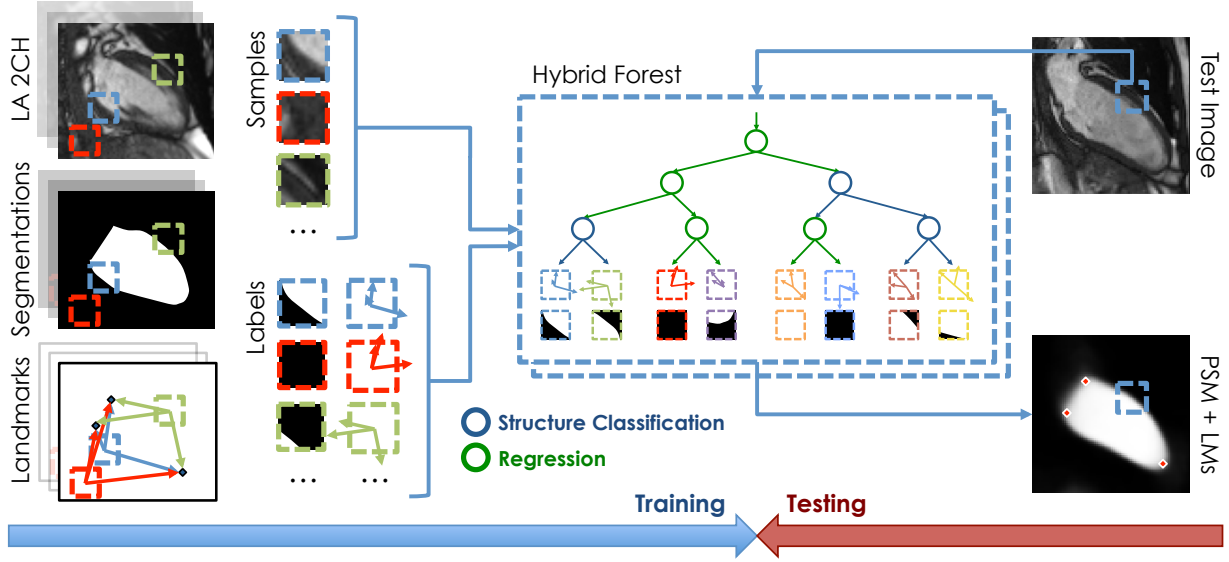


Fig. 3: Hybrid random forest. During training, randomly extracted samples with associated labels, consisting of segmentations and vector displacements, are fed to the forest, and the learnt associations are stored in the leaf nodes. During testing, each sample extracted from the test image is sent to the model, estimating both PSM and LMs at once.

types of nodes (maximizing different information gains) can be interleaved within a single tree structure in order to perform multiple tasks. As in previous approaches [22], [20], in the present technique structured classification nodes (aiming at the detection of an object close to the desired landmarks, in our case usually the LV cavity) and regression nodes (aiming at landmark localization) are combined (see Fig. 3). In particular, in the proposed framework the landmark localization is conditioned on the results of the detection of the cavity [22]. This not only leads to the estimation of two different types of information (PSMs and LMs) with only one model, but improves the landmark localization by implicitly incorporating complementary information about cardiac position and shape.

Structured Classification and PSM Extraction: Structured classification extends the concept of classification by using structured labels for \mathcal{Y} in lieu of integer labels. In our case, each label $\mathbf{y} \in \mathcal{Y}$ (associated to the image patch \mathbf{x}) consists of a segmentation of the LV cavity within \mathbf{x} . To train a structured classification node it is necessary to find a way to cluster structured labels at each split node into two subgroups depending on some similarity measure between them. The solution to this problem was first proposed by Dollar et al. [23] and consists of two steps. First, \mathcal{Y} is mapped to an intermediate space \mathcal{Z} by means of the function $\Pi : \mathcal{Y} \rightarrow \mathcal{Z}$ where the distance between labels can be computed. Importantly, Π must be chosen so that similar labels \mathbf{y} will be associated to vectors \mathbf{z} close to each other with respect to the distance defined in \mathcal{Z} . Then, PCA is applied to the vectors \mathbf{z} to map the associated labels \mathbf{y} into a binary set of labels $c \in \mathcal{C} = \{0, 1\}$, which is achieved by applying a binary quantization to the principal component of each \mathbf{z} vector. Finally, the Shannon entropy can be adopted [23]:

$$H_{sc}(S) = - \sum_{c \in \mathcal{C}} p(c) \log(p(c)), \quad (1)$$

with $p(c)$ indicating the empirical distribution extracted from the training subset at each node. In our previous work [20], this approach has been adopted for structured labels \mathcal{Y} consisting of edge maps (EMs) highlighting the contours of the myocardium. In the case of EMs, the mapping Π can simply encode for each pair of pixels whether they belong to the same segment in the label \mathbf{y} or not:

$$\Pi_{EM} : \mathbf{z} = [\mathbf{y}(j_1) = \mathbf{y}(j_2)] \quad \forall j_1 \neq j_2, \quad (2)$$

where j_1 and j_2 are indices spanning every pixel in \mathbf{y} . The resulting long binary vector can be used to compare this particular label to the other ones by simply computing the Euclidean distance in \mathcal{Z} . However, the same choice for Π cannot be adopted for our task, which aims at using structured labels consisting of segmentation maps (SMs) of the LV cavity. For example, let's imagine two labels \mathbf{y}_1 and \mathbf{y}_2 , the former completely outside the LV cavity and the latter completely inside: using the mapping Π_{EM} , we would obtain $\mathbf{z}_1 = \mathbf{z}_2$, which contradicts the requirement by which only similar labels will be mapped close to each other in \mathcal{Z} . Consequently, we implemented a different mapping:

$$\Pi_{SM} : \mathbf{z} = [\mathbf{y}(j_1) = \mathbf{y}(j_2) = 0] \oplus \dots \oplus [\mathbf{y}(j_1) = \mathbf{y}(j_2) = 1] \quad \forall j_1 \neq j_2, \quad (3)$$

which encodes for each pair of pixels in \mathbf{y} whether they are both equal to 0, whether they are both equal to 1 and then concatenates the two binary vectors. This formulation ensures the proper computation of the distance between labels, and thus to correctly cluster them at each node based on their similarity. At the end of the training process, the label $\hat{\mathbf{y}}$ stored in each leaf node is the one whose $\hat{\mathbf{z}}$ is the medoid (i.e. that minimizes the sum of distances to all the other \mathbf{z} at the same node). At testing time, each sample patch of the test image is sent down each tree of the forest, and the segmentation

maps stored at each selected leaf node are averaged, producing a smooth segmentation map (PSM) of the LV cavity. The values in the PSM are actual probabilities (proportional to the certainty in LV cavity detection), and can be used to assess the reliability of the prediction. Of note, the introduced formulation for Π_{SM} in Eq. 3 could be easily extended to multi-label PSM generation by concatenating additional binary vectors computed for each label c_i and by performing a channel-based averaging operation at testing time.

Regression and Landmark Detection: To train regression nodes, it is necessary to add to each sample patch \mathbf{x} an additional label $\mathcal{D} = (\mathbf{d}^1, \mathbf{d}^2, \dots, \mathbf{d}^L)$, where \mathbf{d}^l represents for each of the L landmarks the N -dimensional displacement vector from the patch centre to the landmark location. Instead of the Shannon entropy defined for structured classification in Eq. 1, regression nodes are trained by minimizing the determinant of the full covariance matrix $|\Lambda(S)|$ defined by the landmark displacement vectors:

$$H_r(S) = \frac{1}{2} \log((2\pi e)^d |\Lambda(S)|). \quad (4)$$

The regression information is stored at each leaf node k using a parametric model following a $N \cdot L$ -dimensional multivariate normal distribution with \mathbf{d}_k^l and Σ_k^l mean and covariance matrices, respectively. At testing time, for each landmark, Hough vote maps are generated by summing up the regression posterior distributions obtained from each tree for each patch (minus normalization factors) [22]. Following the assumption that pixels belonging to the LV are more informative for cardiac landmark detection than background ones, the PSM values for the LV cavity are used for each patch as weighting factor during the generation of the Hough vote maps [20], effectively restricting voting rights only to pixels likely to belong to the LV cavity itself. Finally, the location of a landmark is determined by identifying the pixel with the highest value on each of the L Hough vote maps.

Model Training: Each patch \mathbf{x} is represented by several features: multi-resolution image intensity, histogram of gradients (HoG) and gradient magnitude. For a detailed description, please refer to [20]. The described hybrid random forest approach is used to build five different models (I-V) for our application (see Fig. 2): PSM estimation of LV cavity and LMs localization of apex and mitral valve for LA images, PSM of LV cavity and LV myocardium for SA stacks. For LA 3CH and 4CH images (models II and III) only one mitral valve point is identified because in these images the LV outflow tract of the aorta can partially occlude one side of the mitral valve, making its localization inaccurate. Also, the training of the models using SA images (models IV and V) is performed by feeding the random forests with all the slices extracted from the SA image stacks: consequently, at testing time, the models are applied to each slice of the stack independently.

B. Heart Coverage Estimation

Heart coverage is estimated exploiting the landmarks identified on LA 2CH, 3CH and 4CH images using the previously trained hybrid forest models. The rationale is that a properly scanned SA stack should encompass the whole portion of

Algorithm 1: Heart Coverage Estimation

Input landmarks:

Apex: $\mathbf{l}_1^{2CH}, \mathbf{l}_1^{3CH}, \mathbf{l}_1^{4CH}$

Mitral Valve points: $\mathbf{l}_2^{2CH}, \mathbf{l}_3^{3CH}, \mathbf{l}_2^{3CH}, \mathbf{l}_2^{4CH}$

Change coordinate system:

Apex: $\hat{\mathbf{l}}_1^{2CH}, \hat{\mathbf{l}}_1^{3CH}, \hat{\mathbf{l}}_1^{4CH}$

Mitral Valve points: $\hat{\mathbf{l}}_2^{2CH}, \hat{\mathbf{l}}_3^{3CH}, \hat{\mathbf{l}}_2^{3CH}, \hat{\mathbf{l}}_2^{4CH}$

Compute median landmarks:

$l_a = \text{median}(\hat{\mathbf{l}}_1^{2CH}, \hat{\mathbf{l}}_1^{3CH}, \hat{\mathbf{l}}_1^{4CH})$

$l_m = \text{median}(\hat{\mathbf{l}}_2^{2CH}, \hat{\mathbf{l}}_3^{3CH}, \hat{\mathbf{l}}_2^{3CH}, \hat{\mathbf{l}}_2^{4CH})$

with z-components l_a and l_m , respectively

Extract SA stack extension in the z direction:

Apex: r_a

Base: r_m

Compute coverage CV:

$$CV = \begin{cases} \frac{\max(0, \min(r_a, l_a) - \max(r_m, l_m))}{l_a - l_m} & \text{if (condition)} \\ \frac{r_a - r_m}{l_a - l_m} & \text{otherwise} \end{cases}$$

(condition): $r_a < l_a$ or $r_m > l_m$

space between the apex and the mitral valve. As highlighted in Fig. 2, for a specific subject we identify three landmarks for the apex (one per each LA image: \mathbf{l}_1^{2CH} , \mathbf{l}_1^{3CH} and \mathbf{l}_1^{4CH}) and four for the mitral valve (\mathbf{l}_2^{2CH} , \mathbf{l}_3^{3CH} , \mathbf{l}_2^{3CH} , \mathbf{l}_2^{4CH}) with values in the coordinate systems of each respective LA image. Using the orientation matrix extracted from the DICOM headers of the acquired SA and LA images, it is possible to define the coordinates of these landmarks in the coordinate system of the SA stack itself. Two new ‘‘median’’ landmarks (l_a and l_m) are then defined taking the medians of the coordinates of the landmarks for the apex and for the mitral valve, respectively, in the SA coordinate system. The extension in the z direction (i.e. along the LV long axis) of the SA stack can be easily computed from the slice thickness and slice number, which are stored in the DICOM header of the stack itself: the two extrema along this direction are defined r_a and r_m , respectively. Finally, the relative coverage can be computed by comparing the relative positions along the z direction of l_a and l_m (i.e. the space that is supposed to be covered by the SA stack) to the portion of space between r_a and r_m (i.e. the space that is actually covered). The steps for coverage estimation are listed in Algorithm 1, including the formula for the computation of the coverage (under the assumption that the apex is located at higher z compared to the mitral valve). Importantly, this technique can seamlessly be applied even if only one LA image is available. Also, while minor motion can occur between the acquisitions of LA images and of the SA stack, it is generally negligible in the z direction (the only one influencing coverage) and thus registration procedures between these images were found to be unnecessary.

C. Inter-Slice Motion Detection

Inter-slice motion detection relies on the PSMs extracted from the acquired images. The rationale is that while LV

cavity PSMs of motion-corrupted SA slices are misaligned, PSMs extracted from the LA images represent sections of the true shape of the LV cavity and can consequently be used as reference. Moreover, the amount of misalignment between the SA PSMs and LA PSMs can be used as an indicator of motion. To perform this assessment, the LA PSMs are initially rigidly registered (by 3D translation only, using sum of squared differences as dissimilarity metric) to the SA PSM stack to compensate for potential motion between different acquisitions. Then, for each slice of the SA PSM stack, the three registered LA PSMs are resampled and combined into a single image (referred to as combined LA PSM) containing the sections of the LA PSMs with respect to a specific slice (see Fig. 4). Finally, in-plane rigid registration (by translation only, using sum of squared differences as dissimilarity metric) is performed between each SA PSM slice and the associated combined LA PSM. Of note, this step is performed only on the slices which are effectively covering the LV, condition assessed using the LA LMs as in Algorithm 1. For each slice, the magnitude of the translation that would be required to perform the registration is used as a metric for motion (i.e. differences in breath-holding position). The steps for motion detection are listed in Algorithm 2.

Algorithm 2: Inter-Slice Motion Detection

Input PSMs:

LA images: PSM^{2CH} , PSM^{3CH} , PSM^{4CH}
 SA slices: PSM_s^{SA-Cav} , $s = (1, \dots, numSlices)$

Perform rigid registration of LA PSMs to SA PSM:

Output: \overline{PSM}^{2CH} , \overline{PSM}^{3CH} , \overline{PSM}^{4CH}

for $s = 1$ to $numSlices$ do
Resample LA PSMs:

Output: \overline{PSM}_s^{2CH} , \overline{PSM}_s^{3CH} , \overline{PSM}_s^{4CH}

Combine resampled LA PSMs:

Output: $\overline{PSM}_s^{LA-comb}$

Perform in-plane rigid registration of

PSM_s^{SA-Cav} to $\overline{PSM}_s^{LA-comb}$:

Output: Translation magnitude T_s

end

D. Cardiac Image Contrast Estimation

Cardiac image contrast is estimated using the LV cavity and LV myocardium PSMs extracted from the SA stack. The rationale is to transform the PSMs into hard segmentations (SMs) and to use them to estimate the difference between average pixel intensity in the LV cavity and in the LV myocardium. Each slice of the cavity PSMs is thresholded selecting the N_{cav} pixels with the highest probability values: this will maximize the probability of measuring the intensity in the actual cavity. The same happens to the myocardium PSM, thresholded selecting N_{myo} pixels. To exclude potential spurious regions from the obtained segmentation, the average centroid for the cavity segmentation is computed among the different slices, and for each slice only the connected component closest to the average centroid is kept, both for the cavity

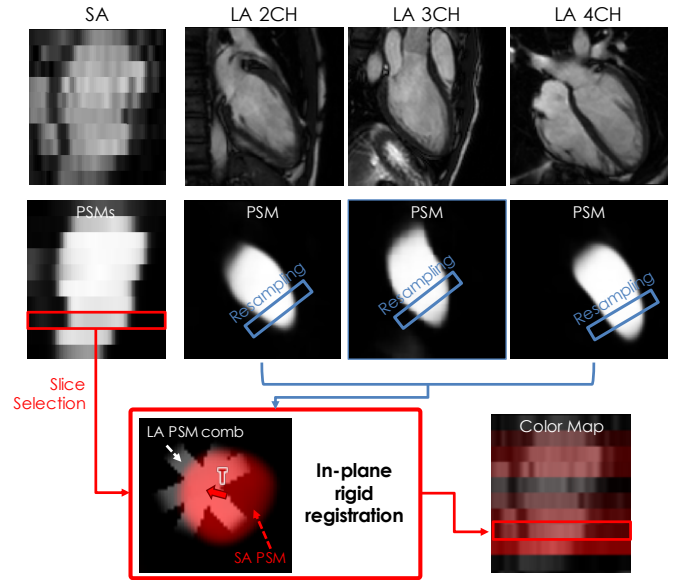


Fig. 4: Motion detection technique. For each slice of the SA stack, the corresponding portion of space in each LA PSM is resampled and combined, producing the “asterisk-shaped” LA PSM comb image. In-plane rigid registration is then performed between each SA PSM and LA PSM comb, and the translation magnitude T used as proxy for inter-slice motion for that slice. A color map, with the intensity of each slice proportional to the respective T , can be also generated.

and myocardial segmentations. Of note, this step is performed taking into account the slice-by-slice rigid transformation estimated using Algorithm 2, which amounts to performing the average centroid computation and connected components analysis on a motion-compensated stack. Finally, in order to exclude potential papillary muscles from the cavity intensity computation, a Gaussian mixture model is fitted to the distribution of intensity values inside the cavity segmentation. Since only some slices show papillary muscles, both a two-component and a one-component models are used, and only one is selected based on the Akaike information criterion [24]. In the event that the two-component model yields the best fit, since the cavity distribution is always higher than that of the papillary muscles, the mean of the component with the highest mean is used as average intensity value for the cavity. For the myocardium, the simple mean intensity of the pixels masked by the segmentation is computed. Cardiac image contrast is finally defined as the difference between these two values. The steps for cardiac image contrast estimation are also listed in Algorithm 3.

E. Performance Evaluation

Image Acquisition: Training and testing of the proposed quality control pipeline were both carried out on randomly-generated subsets of the UKBB dataset. CMR imaging for the UKBB study was performed using a 1.5T Siemens MAGNETOM Aera system equipped with a 18 channels anterior body surface coil (45 mT/m and 200 T/m/s gradient system). 2D cine balanced steady-state free precession (b-SSFP) SA

Algorithm 3: Cardiac Image Contrast Estimation

Input PSMs:

LV cavity: PSM_s^{SA-Cav}
 LV myocardium: PSM_s^{SA-Myo}
 with $s = (1, \dots, numSlices)$

for $s = 1$ **to** $numSlices$ **do****Threshold** PSM_s^{SA-Cav} and PSM_s^{SA-Myo} :Output: SM_s^{SA-Cav} and SM_s^{SA-Myo} **Estimate centroids** P_s **for** SM_s^{SA-Cav} **end****Estimate mean centroid:** $P = \text{mean}(P_s)$ **for** $s = 1$ **to** $numSlices$ **do****Exclude all but one connected component per SM based on distance to P:**Output: \overline{SM}_s^{SA-Cav} and \overline{SM}_s^{SA-Myo} **Fit Gaussian Mixture Model to** \overline{SM}_s^{SA-Cav} **to exclude papillary muscles:**Output: μ_s^{SA-BP} **Compute contrast CT:**

$$CT = \mu_s^{SA-BP} - \text{mean}\left(SA_s\left(\overline{SM}_s^{SA-Myo}\right)\right)$$

with SA_s the s-slice of the SA stack**end**

image stacks were acquired with in-plane spatial resolution 1.8×1.8 mm, slice thickness 8 mm, slice gap 2 mm, image size 198×208 and average number of slices 10. 2D cine b-SSFP LA images were acquired with in-plane spatial resolution 1.8×1.8 mm, slice thickness 8 mm and image size 162×208 . Further acquisition details can be found in [3]. Only end-diastolic frames were considered.

Experimental design: A series of experiments were conducted to assess the accuracy of each of the three quality control checks. First, the five hybrid random forest models were trained. For each LA image-based model, 500 images were used, together with manually-annotated landmarks and segmentations of the LV cavity. Each training set was quadrupled in size through data augmentation applying random rescaling following a normal distribution ($\mu = 1$, $\sigma = 0.1$) and random rotation ($\mu = 0^\circ$, $\sigma = 30^\circ$). For each of the two SA stack-based models, the slices extracted from 500 stacks were used (for a total of 5165 images), together with segmentations of the LV cavity and of the LV myocardium, respectively. Details regarding forest training include image patch size 48×48 px for LA models and 32×32 px for SA ones, segmentation label size 16×16 px, number of samples $4 \cdot 10^6$, number of trees $T = 8$. The five hybrid random forest models were then applied to a testing set consisting of 3000 subjects randomly extracted from the UKBB.

To evaluate the accuracy of the proposed heart coverage estimation technique two experiments were conducted. First, for each of the three LA views, the positions of the landmarks were manually annotated on 100 randomly selected images. The automatically detected landmarks were compared to the manually identified ones by measuring the Euclidean distance between the two sets of points. Then, the 3000 SA stacks were

visually inspected (sometimes using LA images as reference) to identify cases with insufficient coverage, defined as such when at least one slice was missing (in either the basal or apical direction). Automated heart coverage estimation was then performed on the same dataset. To detect cases for which the landmark detection failed, a sanity check was performed: for each LA view, when either of the relative distances between the landmarks was over 2 standard deviations greater or smaller than the respective mean distance value (as computed on a separate set of 200 images), the landmarks from that image were discarded, and the automated coverage estimation was performed only on the remaining landmarks (if available). Finally, the accuracy of the technique was assessed against the performed visual inspection with an ROC analysis. A standard binary classification test was also performed: following the criterion presented for visual inspection and considering that the SA stacks consisted on average of 10 slices, a coverage value of less than 90% was used as threshold for insufficient coverage.

To evaluate the accuracy of the motion detection technique, 1500 SA stacks were visually inspected (sometimes using LA images as reference) to identify cases with noticeable motion corruption. Automated motion detection was then performed on the same dataset. To detect cases for which the PSM estimation failed, a sanity check was performed: for each stack, PSM slices (whose values range between 0 and 1024) with a peak probability value below a user defined threshold set to 600 were considered not reliable for motion detection, and thus their T_s (i.e. the estimated translation magnitude) discarded; if less than 2 T_s values were left, the motion detection analysis was not performed on the specific stack. Accuracy of the automated technique was assessed against visual inspection with a standard binary classification test using the following criterion: a stack was deemed motion-corrupted if either the average T_s was above a first threshold T_A or at least two T_s were above a second threshold T_B . This double criterion aimed at the detection of both stacks with a few, clearly misaligned slices as well as stacks with poor general alignment. Both T_A and T_B were optimized automatically using an ROC-like approach.

To evaluate the accuracy of the cardiac image contrast estimation technique, 100 random slices from as many random SA stacks were manually annotated selecting regions of interests (ROIs) within the LV cavity and the LV myocardium. Cardiac image contrast was estimated both from the original images and from the images after contrast normalization using a randomly selected reference image stack. Automated contrast estimation was then performed on the same dataset, both before and after normalization. For each slice, a sanity check was performed: if either the peak value of either of the two PSMs was below 150 or the size of either of the segmentations \overline{SM}_s^{SA-Cav} and \overline{SM}_s^{SA-Myo} was less than 10 pixels, the obtained contrast was deemed unreliable and excluded from the analysis. Automatically estimated and manually computed contrast values were compared using Pearson's correlation coefficient, linear regression and Bland-Altman analyses.

Landmark Detection				
Localization Error	LA 2CH	LA 3CH	LA 4CH	
Apex	4.2 ± 2.5	4.5 ± 3.0	4.6 ± 3.1	
Mitral Valve (Side I)	3.6 ± 2.6	3.5 ± 2.6	3.2 ± 2.3	
Mitral Valve (Side II)	3.9 ± 2.7			

TABLE I: Landmark localization errors in mm (mean ± std).

Heart Coverage Estimation					
SE	SP	Visual Assessment			
88%	99%	Proposed Technique	49 (TP)	15 (FP)	
			7 (FN)	2926 (TN)	

TABLE II: Sensitivity, specificity and confusion matrix for heart coverage estimation using a 90% coverage threshold. Positive cases correspond to cases with insufficient coverage.

IV. RESULTS

The experiments were initially run on a single core of an Intel Xeon CPU E5-1650 v3 @ 3.50GHz with 64 GB of memory to assess the speed of the current pipeline. Average time required to extract PSMs and LMs (when included in the model) was 1.3s per SA stack (of roughly 10 slices) and 0.85s per LA image. Average times required to perform the quality control checks were 0.26s per SA stack for coverage estimation, 9s per SA stack for motion detection (in this case using parallelization on 6 cores to evaluate multiple slices from one stack at once) and 0.6s per slice for contrast estimation. The localization errors for landmark detection for the three LA views are reported in Table I. Of note, the landmarks extracted from one image per LA view were identified as outliers and thus excluded from the reported results. For accuracy assessment of heart coverage estimation, 3 of the 3000 cases were excluded from the analysis: one due to the lack of LA images, and two for failing the sanity check on all the LA images. The ROC analysis performed on the remaining 2997 images yielded an area-under-curve AUC = 0.97. The results of the binary classification test, obtained after fixing the coverage threshold to 90%, are reported in Table II. For accuracy assessment of motion detection, 3 of the 1500 cases were excluded from the analysis: one due to the lack of the SA stack and two for failing the sanity check. An ROC-like analysis was performed on the remaining 1497 images to select the thresholds T_A and T_B . The results of the binary classification test, obtained for $T_A = 3.4$ mm and $T_B = 6$ mm, are reported in Table III. For accuracy assessment of contrast estimation, 3 of the 100 images were excluded from the analysis for failing the sanity check. Results for Pearson’s correlation coefficient, linear regression and Bland-Altman analyses between automatically and manually estimated contrast values are reported in in Table IV.

Examples of the results obtained with the three checks are shown in Figs. 5, 6 and 7.

V. DISCUSSION

The results obtained for the landmark detection experiment show that the average localization error is around 3.9 mm

Inter-Slice Motion Detection					
SE	SP	Visual Assessment			
85%	95%	Proposed Technique	213 (TP)	58 (FP)	39 (FN)
				1187 (TN)	

TABLE III: Sensitivity, specificity and confusion matrix for motion detection using $T_A = 3.4$ mm and $T_B = 6$ mm. Positive cases correspond to motion-corrupted cases.

Cardiac Image Contrast Estimation						
	R	Bias	Std	a	b	Mean
Original Images	0.95	-0.6	12.1	0.96	7.8	190
Normalized Images	0.94	-0.7	12.4	0.97	5.3	169

TABLE IV: Pearson’s correlation coefficient (R), bias and std for Bland-Altman analysis, regression coefficients (a and b) for the linear regression analysis and mean measured value between automatically and manually estimated cardiac image contrast, both on original images and after histogram normalization, all reported in arbitrary values.

(roughly two pixels) and is thus small compared to the reconstructed slice thickness (10 mm), suggesting the reliability of the landmark detection technique for the sake of heart coverage estimation. The binary classification test on coverage estimation performed on 2997 cases indicates the high accuracy of the proposed technique, with sensitivity = 88% and specificity = 99%. The interpretation of these results is hindered by the strong class imbalance between cases with sufficient and insufficient coverage, and thus a more detailed analysis of the reported confusion matrix is required. By applying the proposed automated technique, it is possible to correctly detect 88% of the cases with insufficient coverage, and thus to lower the percentage of undetected wrongly imaged cases from 1.9% to 0.2%. This comes at the price of having to visually check an additional 0.5% of cases that actually featured a sufficient coverage. Notably, several of the 15 FP cases actually had a sub-optimal coverage, but not of the amount required to be considered as wrongly imaged following the criterion adopted during visual inspection. Compared to our previous work [11], the present approach makes use of three LA images instead of just one. The redundancy offered by exploiting all the available LA views allows a more robust and reliable estimation: this is suggested by the higher sensitivity and specificity achieved (88% vs 73% and 99% vs 98%, respectively, although a direct comparison is not completely fair since the UKBB subset used in [11] was different from the present one) and by the lower number of cases excluded due to failing the sanity check (down from 89 to 3). Of note, this check is able to indirectly detect and exclude LA images with high noise levels, wrong acquisition planning or wrong file naming that make the landmark localization unreliable, and in the present implementation only cases in which all the three LA views yielded bad landmark detection had to be excluded from the coverage assessment. Comparing the accuracy of the proposed approach to that presented by Zhang et al. [9], performing CNN-based slice classification of most basal and

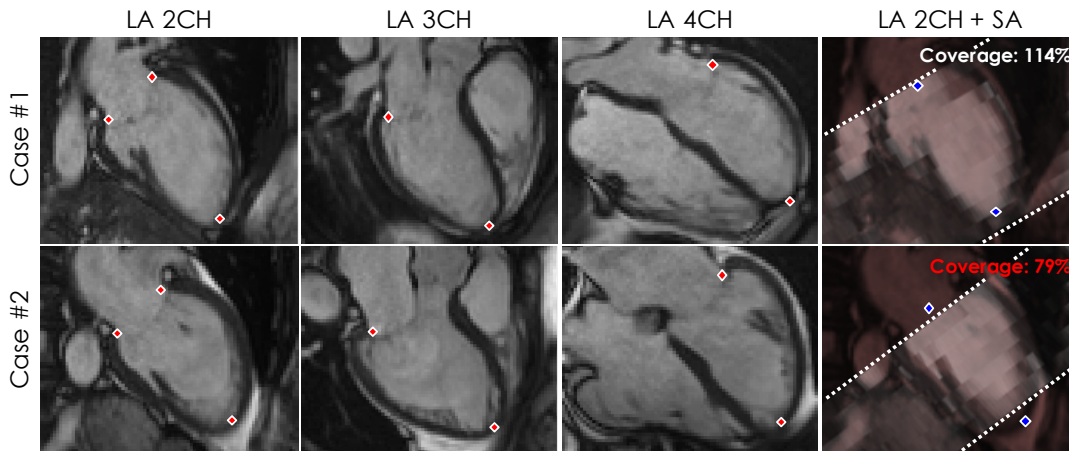


Fig. 5: Results for heart coverage estimation in two cases, one with sufficient (case #1) and one with insufficient coverage (case #2). In the first three columns, the results for landmark detection in the three LA views. In the last column, a mix view with LA two-chamber view and the SA stack together with the median landmarks for the mitral valve and the apex.

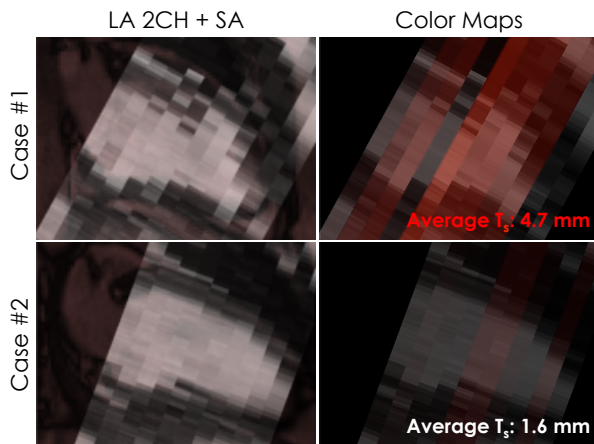


Fig. 6: Results for motion detection in two cases, one with (case #1) and one without motion corruption (case #2). In the second column, the color maps of the translation magnitude for each slice are overlaid on top of the SA stacks.

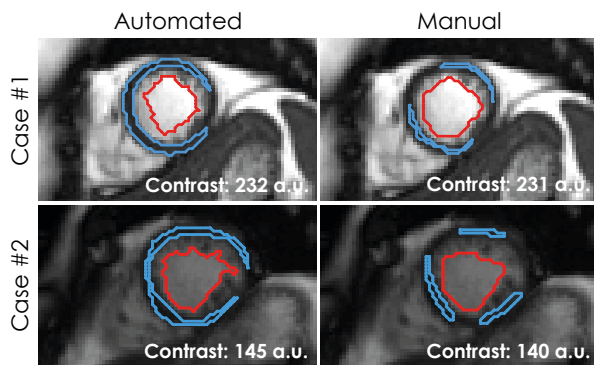


Fig. 7: Results for contrast estimation in two cases, one with high (case #1) and one with low contrast (case #2). The ROIs from which the mean intensities are estimated are shown in red and cyan, respectively.

most apical slices (reporting an average accuracy of 77% and 75%, respectively), is not feasible due to the differences in the adopted validation strategies. However, it is worth noting that our approach is not affected by the strong class imbalance for heart coverage hindering their approach: to mitigate this limitation, the authors have increased the training dataset size using generative networks [10] (reaching average accuracies of 93% and 89%, respectively), which are nonetheless known to be affected by training instability. Moreover, we believe that there is a clinical and practical advantage in measuring the relative coverage instead of performing a binary classification: cases with only slightly sub-optimal coverage could still be included in the following analyses, especially when the lack of coverage is in the apical area.

The reported results for motion detection indicate that the proposed approach achieves sensitivity = 85% and specificity = 95% over 1497 cases. By applying the proposed automated technique, it is possible to lower the percentage of undetected motion-corrupted cases from 16.8% to 2.6%. This comes at the price of having to visually check 3.9% cases that were visually deemed motion-free. It's worth to note that the binary classification of stacks based on the visual assessment of motion is a difficult task in itself, limiting the measurable accuracy of any technique. A more thorough examination would require a slice-by-slice visual classification, which is however impractical for datasets of this size.

The accuracy of the contrast estimation technique is indicated by very high correlation coefficients and regression lines near unity both for images before and after contrast normalization. Bland-Altman analyses show negligible biases and narrow limits of agreement with respect to the mean measured values, suggesting the high accuracy of the technique.

Our approach to quality control does not attempt to directly classify sub-optimal cases like other techniques [9] for two reasons. First, it allows the complete circumvention of any class-imbalance issues, since the only learning-based portions of our pipeline aim at the identification of structures that are present in every image. Second, the implemented pipeline does

not constitute a “black-box” approach: every quality check produces quantitative metrics with a clear meaning, which can be of great value in informing the MR operators about the type and entity of the identified issues.

The main limitation affecting our approach is that no quality check is performed on the manual selection of the imaging planes for the LA views, which can be subject to error. However, countermeasures have been implemented to deal with this issue. Regarding coverage estimation, the redundancy offered by exploiting all the three LA views and the adoption of a sanity check helps in minimizing this issue. Regarding motion detection, a slightly off-axis LA image still correctly represents the cardiac anatomy, and the initial 3D registration step will position it correctly with respect to the SA stack.

VI. CONCLUSION

In this paper a fully-automated learning-based pipeline for quality control of CMR images has been presented. The implemented quality checks are heart coverage estimation, interslice motion detection and cardiac image contrast estimation for short-axis image stacks. The pipeline uses hybrid random forests to extract probabilistic segmentation maps and identify landmarks on long- and short-axis images, and then leverages these information to perform the quality checks. It was tested on up to 3000 cases from the UKBB study and compared to the results of visual or manual analyses to evaluate its accuracy. The results suggest that the proposed approach is able to perform the quality checks with a high accuracy. With the recent launch of several initiatives for the acquisition of large-scale CMR datasets, there is a strong need for robust quality control tools in order to facilitate and ensure the reliability of the analyses performed as part of clinical studies. In addition, the low computational time required by the proposed pipeline makes it potentially deployable at the acquisition site, allowing the almost real-time assessment of the scan and the potential triggering of a new acquisition.

ACKNOWLEDGMENTS

This research has been conducted using the UK Biobank Resource [3] under Application Number 18545. The first author benefited from a Marie Skłodowska-Curie Fellowship.

REFERENCES

- [1] J. Zhuo and R. P. Gullapalli, “MR Artifacts, Safety, and Quality Control,” *RadioGraphics*, vol. 26, no. 1, pp. 275–297, jan 2006.
- [2] P. F. Ferreira, P. D. Gatehouse, R. H. Mohiaddin, and D. N. Firmin, “Cardiovascular magnetic resonance artefacts,” *Journal of Cardiovascular Magnetic Resonance*, vol. 15, no. 1, p. 41, 2013.
- [3] S. E. Petersen, P. M. Matthews, J. M. Francis, M. D. Robson, F. Zemrak, R. Boubertakh, A. A. Young, S. Hudson, P. Weale, S. Garratt, R. Collins, S. Piechnik, and S. Neubauer, “UK Biobank’s cardiovascular magnetic resonance protocol.” *Journal of cardiovascular magnetic resonance : official journal of the Society for Cardiovascular Magnetic Resonance*, vol. 18, no. 1, p. 8, jan 2016.
- [4] V. Klinke, S. Muzzarelli, N. Lauriers, D. Locca, G. Vincenti, P. Monney, C. Lu, D. Nothnagel, G. Pilz, M. Lombardi, A. C. van Rossum, A. Wagner, O. Bruder, H. Mahrholdt, and J. Schwitter, “Quality assessment of cardiovascular magnetic resonance in the setting of the European CMR registry: description and validation of standardized criteria,” *Journal of Cardiovascular Magnetic Resonance*, vol. 15, no. 1, p. 55, jun 2013.
- [5] P. Coupé, J. V. Manjón, E. Gedamu, D. Arnold, M. Robles, and D. L. Collins, “Robust Rician noise estimation for MR images,” *Medical Image Analysis*, vol. 14, no. 4, pp. 483–493, 2010.
- [6] I. I. Maximov, E. Farrher, F. Grinberg, and N. Jon Shah, “Spatially variable Rician noise in magnetic resonance imaging,” *Medical Image Analysis*, vol. 16, no. 2, pp. 536–548, 2012.
- [7] E. L. Gedamu, D. L. Collins, and D. L. Arnold, “Automated quality control of brain MR images,” *Journal of Magnetic Resonance Imaging*, vol. 28, no. 2, pp. 308–319, aug 2008.
- [8] X. Albà, K. Lekadir, M. Pereañez, P. Medrano-Gracia, A. A. Young, and A. F. Frangi, “Automatic initialization and quality control of large-scale cardiac MRI segmentations,” *Medical image analysis*, vol. 43, pp. 129–141, jan 2018.
- [9] L. Zhang, A. Gooya, B. Dong, R. Hua, S. E. Petersen, P. Medrano-Gracia, and A. F. Frangi, “Automated Quality Assessment of Cardiac MR Images Using Convolutional Neural Networks,” in *SASHIMI*. Springer, Cham, oct 2016, vol. LNCS, no. 9968, pp. 138–145.
- [10] L. Zhang, A. Gooya, and A. F. Frangi, “Semi-supervised Assessment of Incomplete LV Coverage in Cardiac MRI Using Generative Adversarial Nets Chapter,” *SASHIMI*, vol. LNCS, pp. 138–145, 2017.
- [11] G. Tarroni, O. Oktay, W. Bai, A. Schuh, H. Suzuki, J. Passerat-Palmbach, B. Glocker, A. de Marvao, D. O’Regan, S. Cook, and D. Rueckert, “Learning-Based Heart Coverage Estimation for Short-Axis Cine Cardiac MR Images,” *FIMH*, vol. LNCS, no. 10263, pp. 73–82, jun 2017.
- [12] J. Lötjönen, M. Pollari, S. Kivistö, and K. Lauerma, “Correction of Movement Artifacts from 4-D Cardiac Short- and Long-Axis MR Data,” *MICCAI*, vol. LNCS, no. 3217, pp. 405–412, sep 2004.
- [13] O. Oktay, G. Tarroni, W. Bai, A. de Marvao, D. P. O’Regan, S. A. Cook, and D. Rueckert, “Respiratory motion correction for 2D cine cardiac MR images using probabilistic edge maps,” in *Computing in Cardiology Conference (CinC)*. IEEE, 2016, pp. 129–132.
- [14] M. Sinclair, W. Bai, E. Puyol-Antón, O. Oktay, D. Rueckert, and A. P. King, “Fully Automated Segmentation-Based Respiratory Motion Correction of Multiplanar Cardiac Magnetic Resonance Images for Large-Scale Datasets,” *MICCAI*, vol. LNCS, Part, no. 10434, pp. 332–340, sep 2017.
- [15] D. Yang, P. Wu, C. Tan, K. M. Pohl, L. Axel, and D. Metaxas, “3D Motion Modeling and Reconstruction of Left Ventricle Wall in Cardiac MRI,” in *Functional Imaging and Modeling of the Heart*, vol. LNCS 10263. Springer, Cham, jun 2017, pp. 481–492.
- [16] K. McLeish, D. L. G. Hill, D. Atkinson, J. M. Blackall, and R. Razavi, “A study of the motion and deformation of the heart due to respiration.” *IEEE transactions on medical imaging*, vol. 21, no. 9, pp. 1142–50, sep 2002.
- [17] O. Dietrich, J. G. Raya, S. B. Reeder, M. F. Reiser, and S. O. Schoenberg, “Measurement of signal-to-noise ratios in MR images: Influence of multichannel coils, parallel imaging, and reconstruction filters,” *Journal of Magnetic Resonance Imaging*, vol. 26, no. 2, pp. 375–385, aug 2007.
- [18] S. Aja-Fernández, G. Vegas-Sánchez-Ferrero, and A. Tristán-Vega, “Noise estimation in parallel MRI: GRAPPA and SENSE,” *Magnetic Resonance Imaging*, vol. 32, no. 3, pp. 281–290, apr 2014.
- [19] S. D. Wolff and R. S. Balaban, “Assessing contrast on MR images.” *Radiology*, vol. 202, no. 1, pp. 25–29, jan 1997.
- [20] O. Oktay, W. Bai, R. Guerrero, M. Rajchl, A. de Marvao, D. P. O’Regan, S. A. Cook, M. P. Heinrich, B. Glocker, and D. Rueckert, “Stratified Decision Forests for Accurate Anatomical Landmark Localization in Cardiac Images,” *IEEE Transactions on Medical Imaging*, vol. 36, no. 1, pp. 332–342, jan 2017.
- [21] A. Criminisi, J. Shotton, and E. Konukoglu, “Decision Forests: A Unified Framework for Classification, Regression, Density Estimation, Manifold Learning and Semi-Supervised Learning,” *Foundations and Trends® in Computer Graphics and Vision*, vol. 7, no. 2-3, pp. 81–227, 2011.
- [22] J. Gall, A. Yao, N. Razavi, L. Van Gool, and V. Lempitsky, “Hough Forests for Object Detection, Tracking, and Action Recognition,” *IEEE Transactions on Pattern Analysis and Machine Intelligence*, vol. 33, no. 11, pp. 2188–2202, nov 2011.
- [23] P. Dollar and C. L. Zitnick, “Fast Edge Detection Using Structured Forests,” *IEEE Transactions on Pattern Analysis and Machine Intelligence*, vol. 37, no. 8, pp. 1558–1570, 2015.
- [24] G. Celeux and G. Soromenho, “An entropy criterion for assessing the number of clusters in a mixture model,” *Journal of Classification*, vol. 13, no. 2, pp. 195–212, sep 1996.